Research Paper

Time-domain "wave" model of the human tympanic membrane

Pierre Parent [a,*], Jont B. Allen [b]

[a] Mimosa Acoustics, Inc., 335 Fremont Street, Champaign, IL 61820, USA
[b] University of Illinois at Urbana-Champaign, Department of Electrical and Computer Engineering, Beckman Institute, Room 2061, 405 North Mathews, Urbana, IL 61801, USA

ARTICLE INFO

ABSTRACT

Middle ear models have been successfully developed for many years. Most of those are implemented in the frequency domain, where physical equations are more easily derived. This is problematic, however, when it comes to model non-linear phenomena, especially in the cochlea, and because a frequency-domain implementation may be less intuitive. This research explores a different approach, based on a time-domain implementation, fitted to impedance data. It is adapted from a previous work for the cat and focuses here on the human ear: volume velocity samples are distributed uniformly in space and updated periodically to simulate the propagation of the sound wave in the ear. The modeling approach is simple, yet it can quantitatively reproduce the major characteristics of the human middle ear transmission, and can qualitatively capture forward and reverse power transmission – a key feature of this time-domain implementation. These results suggest that complex, multi-modal propagation observed on the TM may not be critical to proper sound transmission along the ear. Besides, model predictions reveal that impedance and velocimetry measurements may be inconsistent with each other, hypothetically because velocimetry protocols could alter the middle ear.

1. Introduction

1.1. Previous work

Modeling the ear has been a path to refine our understanding of the hearing process. With the development of powerful computational tools, different theories have been studied in order to better understand the ear behavior and isolate the role of its components. The previously-published models can be classified into two broad categories: lumped-parameter models, and distributed models. Each of these may be implemented in either the time or frequency-domain.

Lumped-parameter models use the analogy between acoustic systems and the conventional electrical circuit representation. Each physical element is then represented by a simple association of basic circuit components: mass elements (e.g., bones) are modeled as inductors, stiffness as capacitors (e.g., ligaments) and friction as resistors. This approach has been first used to model the cochlea (Wegel and Lane, 1924). A key work in the field was later presented by Zwislocki (1957, 1962): his approach was to model the entire ossicular chain (OC) of the cat by a frequency-domain lumped-parameter circuit with parameters adjusted to match actual imped-

ance measurements. In order to reduce the number of parameters to adjust simultaneously, the complexity of the model was increased step by step, starting from limited subsystems (e.g., disarticulated stapes experiment) to the fully functional ear. This method has also been used by Lynch et al. (1982). These models are particularly relevant to simulate simple physical elements which can easily be approximated by basic circuit analogies; however, they are not suitable to model more complex distributed structures with large delays, like the tympanic membrane (TM) and when so used, can be inaccurate above a few kilohertz. Shaw's 1977 model of the TM as a double-piston source (Shaw, 1977; Shaw and Stinson, 1981) enabled his model to produce a modal TM response, but limited both in its accuracy and its upper cut-off frequency (e.g., 6 kHz). Puria and Allen (1998) and O'Connor and Puria (2008) circumvented this limitation by associating a lumped-parameter model for the OC with a transmission line modeling the TM.

Wave digital filters are a refinement of this transmission line approach. Such filters are obtained by transforming the analog circuit so that it does not process state variables (pressure and volume velocity) but wave variables (forward and backward components of the wave). Their main theoretical interest is that the structure directly deals with the wave components and can be designed to be much more computationally efficient than conventional circuits. Wave digital filters have been successfully applied to model the hearing path (Giguere and Woodland, 1994) but the resulting model topology is quite far from physical reality, and therefore lacks obvious intuition.

* Corresponding author. Address: 129 avenue du General Leclerc, 75014 Paris, France.
E-mail addresses: pierre@mimosaacoustics.com (P. Parent), jontalle@uiuc.edu (J.B. Allen).

Distributed models may be used to accurately simulate more complex anatomical structures of the TM. Typically, those models rely on a finite elements analysis (FEA), or an asymptotic approach (Funnel and Laszlo, 1978; Rabbitt and Holmes, 1986; Funnel et al., 1987). A clear strength of FEA models is that they can account for complex mechanical and physical constraints by their detailed representations of the eardrum structure. Their main drawbacks reside in their complexity, especially to generate the mesh representing the 3-D structure to be analyzed, as well as their greater computational time. A closely related model of the cat TM using shell theory has been presented by Fay (2001) and Fay et al. (2002).

1.2. Time-domain model

Most of these published models are implemented in the frequency domain. This is relevant because equations describing the wave propagation are typically defined there and lumped circuit elements are easier to deal with (variables are related by frequency-dependent multiplications instead of time-domain convolutions). However, frequency-domain models are inherently limited, or even fail, when dealing with non-linear and/or time-varying phenomena, which can only be modeled in the time domain. Time dependent non-linearities are critical, both in the middle ear, and the cochlea (Sen and Allen, 2006). Also, time-domain models are especially convenient when modeling large-delays systems, such as the TM. Those models can be made more intuitive and can lead to sparse, recursive, computationally efficient implementations. For example, the wave model of Kelly and Lochbaum (1963) is a well-known and highly successful model of the time-varying vocal tract.

This study aims at exploring such a wave-based model design for the human middle ear. Eventually, we suspect such a model could be easier to implement and interpret, and could also provide an important simulation tool to study non-linear and time-varying behavior. Such a model has already been published for the cat (Parent and Allen, 2007) and is extended here to the normal human ear, and to several common pathologies. A this early stage in the model development, the goal is not to compete with the extent and accuracy of previously-published models, but rather to demonstrate that a time-domain approach is feasible, and that it provides more physical insight about wave propagation in the middle ear. We hope that future work in this direction will improve the model accuracy and predictive power.

This approach is particularly relevant in discriminating between the forward and backward wave components. This more detailed description enables us to compute propagation delays on the forward/backward components, and on the total wave (sum of the two components). These delays are distinct, but related to the modal delays measured from pressure and velocity measurements, and represent different (more precise) estimates of the wave front propagation time.

1.3. Velocimetry and impedance

Experimental measurements of the middle ear may be divided into two broad categories. Velocimetry experiments consist of measuring the displacement or velocity of specific elements of the middle ear (typically, ossicles) while stimulated by a canal or free-field sound source. Those measurements are usually difficult, requiring surgical operation of the target ear to place the probe or measurement device in the ossicles chain. In general, they are carried out on dead temporal bones that have been frozen, or on live subjects during implant operations.

The alternative approach is to leave the middle ear space untouched and to infer its status from a pressure measurement in the ear canal, as done with clinical impedance measurements (e.g., either tympanometry or wideband reflectance). In these cases, the idea is to rely on a specific protocol and a specially calibrated instrument to estimate the input impedance of the ear and assess its status (Stinson et al., 1982; Allen, 1986). The disadvantage of such methods is that they cannot directly estimate the vibrations of the different elements of the middle ear, but only evaluate and infer its behavior as a whole. A further disadvantage is the need for a verifiable model of the ear canal impedance, so as to allow for the interpretation of the clinical impedance measurements. The advantage is that they are non-invasive and they evaluate the ear in its normal condition, on large number of ears, on a clinical basis.

The model presented here is based on such canal impedance measurements, and is designed to match both normal and pathological ears. In order to further validate the model, we also compare its results to velocimetry measurements carried out in temporal bones. We will focus our comparison on the measurements reported by O'Connor and Puria (2008), who have presented a similar model for the human middle ear, but implemented in the frequency domain. Their model results show good agreement with their velocimetry measurements, but not with any canal impedance data. Since our model has been designed to match impedance data, it is interesting to see if we find the reciprocal discrepancy with velocimetry that they find with impedance.

2. Methods

2.1. Presentation of the wave model

This section reviews the basic principles of the implementation, but the reader is referred to the original article for the full details (Parent and Allen, 2007). The model assumes a single-dimension propagation of forward and backward plane waves. The classical plane wave solution of the d'Alembert wave equation stipulates that the propagating volume velocity wave is the sum of two components: one going in the forward direction (from the canal to the cochlea, say from left to right in our representation), and one backward. Each velocity component is then represented by a vector of samples representing the amplitude of the plane wave at various positions in the propagation path. This model is based on reflectance; i.e., its parameters are adjusted so that it matches reflectance data measured on normal human ears by Voss and Allen (1994).

The transformation of the amplitude sample from one position to the next depends on the local physical characteristics of the propagation medium. In the simplest case, the medium is homogeneous and the wave propagates unaltered, except for a small (e.g., 0.01%) attenuation to simulate viscous and thermal losses. Such is the case of the ear canal, which is approximated by a straight, air-filled cylinder – a valid approximation for the range of relevant frequencies (Stinson, 1985). A high sampling frequency is chosen, appropriate for the more complex phenomena on the TM and in the OC, then after each sampling period, the velocity amplitude at a given position is transferred to its direct neighbor (Parent and Allen, 2007). The same procedure occurs simultaneously on the forward and backward wave vectors. The forward path is fed at its input by the stimulus signal (here, a unity pulse) and the time reflectance is retrieved from the first (leftmost) sample of the backward wave. The propagation on the TM and in the OC is more complex and is described in the next sections.

It is difficult to reliably estimate the canal length from clinical canal pressure measurements. Voss and Allen (1994) found an average estimated length of 6.6 mm, with a standard deviation of 3.4 mm (measurements on 10 live human subjects). In our model, this length is roughly equivalent to the distance "under" the TM
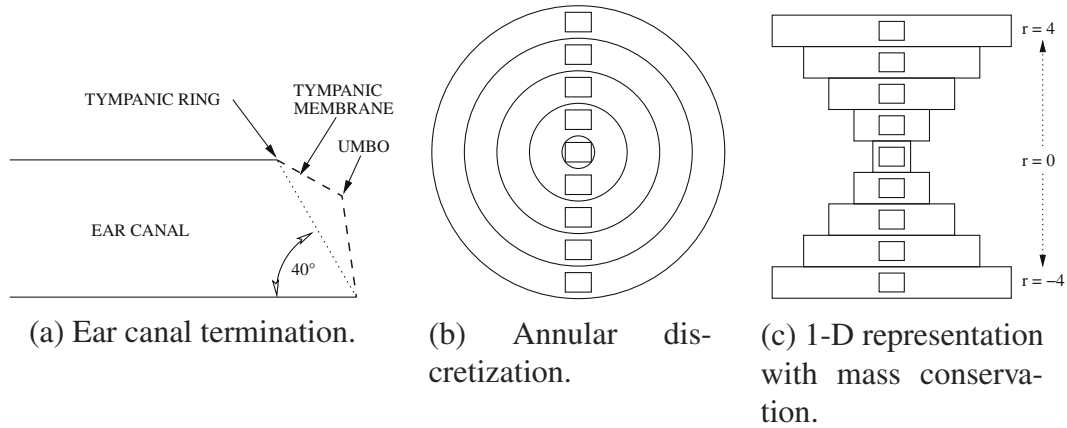
Fig. 1. Discretized tympanic membrane model for $N = 5$. (a) Position of the TM in the ear canal. (b) The decomposition in annuli, respecting the circular geometry of the membrane. (c) The one-dimension model that we actually use, derived from the previous one by applying mass conservation, indicated by the different widths of the stripes. The number of samples on the TM is $2N - 1$, i.e., 9 in this example with $N = 5$. (a) Ear canal termination. (b) Annular discretization. (c) 1-D representation with mass conservation.

(see Fig. 1a), so we have set our canal length before reaching the upper tip of the TM to 1 mm. Under some conditions, when matching specific data sets, we have used slightly different values.

The original model for the cat was fitted to impedance data from Allen (1986). It was then compared to ossicles displacements measurements from Guinan and Peake (1967). Since this is not a ad-hoc model, the numerical values used for the various parameters have not been chosen with the sole objective to match experimental data: rather they have been adjusted to get the best match, but constrained to be similar to previously-published values (Lynch et al., 1982; Puria and Allen, 1998), and to make physically sense. The numerical values used for the present human model have been modified to take into account the anatomical differences between the two species. Some parameters are readily available (canal dimensions, TM area, stapes footplate area) but many unknown middle ear parameters have been derived from the cat's by applying a scale factor, defined by the ratio of the TM areas for each species, $\sqrt{A_{tm}^h / A_{tm}^c}$. The stiffness and resistances have then been adjusted manually to fit experimental data, constrained by a physical range of variation.

2.2. Tympanic membrane model

The TM is positioned at an angle at the canal termination, as shown in Fig. 1a. This angle has been estimated in the human model from measurements of the ear canal diameter and the TM area. Today it is commonly recognized that, in mammals, the TM brings a significant delay (Olson, 1998), which could be accounted for, in part, by a reduced speed of sound on the eardrum (Puria and Allen, 1998). No direct delay measurements in the human are available to our knowledge[1], so the speed of sound on the TM has been manually adjusted so that our model fits the experimental data. We have eventually used a speed on the TM which is 1.5 times slower than in the canal. For comparison, our cat model uses a factor of 3.4.

We demonstrate this result using a one-dimension plan-wave transmission line approximation. An element of the TM is represented by an association of per unit length series mass M and shunt stiffness K, defining the propagation factor

$$\Gamma = s\sqrt{MK}, \tag{1}$$

where s is the Laplace frequency. The speed of sound on the TM c_{tm} is then defined by

$$\Gamma = \frac{s}{c_{tm}}, \tag{2}$$

thus

$$c_{tm} = \frac{1}{\sqrt{MK}}. \tag{3}$$

Since the TM density and stiffness are greater than in air, it is necessary that $c_{tm} < c_{air}$.

Following the suggestion from Puria and Allen (1998), that the TM could be represented by a series of N concentric annuli of varying impedance, we show the intermediate representation of Fig. 1b: each annulus has a different impedance due to the varying curvature of the TM, which ranges from the ear canal impedance at the periphery to the middle ear impedance at the center. This is our hypothesis to explain the impedance-matching role of the TM. Note that the TM is not exactly circular, nor symmetric, but this representation is relevant from the modeling point of view. A circular representation would require a two-dimension processing, which we avoid in this study: it is then further simplified into the one-dimension model of Fig. 1c, where the width of the stripes corresponds to the equivalent area of the corresponding annulus. When input onto the TM, samples are scaled depending on those areas, so that more energy is fed at the periphery than at the center.

The impedance function on the TM surface is hard to directly estimate and, to our knowledge, it has not been investigated. As a first attempt, for the cat, we have assumed an exponential variation from the periphery to the center, the periphery being matched to the canal and the center being matched to the middle ear. This impedance distribution is also assumed symmetric with respect to the TM center. The middle ear impedance has been estimated to be 30 times greater than in the canal (Bekesy and Rosenblith, 1951) and so the transformer ratio brought by the TM is $30/N_{lr}^2$, where N_{lr} is the OC lever ratio (Guinan and Peake, 1967). It is not certain that these assumptions apply to the human ear, but motivated by our cat model we have nonetheless used the same derivation for the human reflection function. Note that this reflection function is not to be considered as a definitive model for the TM; in fact, it is merely a predictive stepping stone, used for the lack of experimental data. This approximation is justified by the similarities between the two species and is confirmed by the success of our

---

[1] Some inferences of this delay have recently become available, based on standing wave patterns measured using various laser measurements (de La Rochefoucauld and Olson, 2009; Cheng et al., 2009).

results. We refer the reader to our original model (Parent and Allen, 2007) for a more detailed discussion on the TM impedance function.

Due to the TM inclination, the canal cross-section area tends to zero towards its termination, resulting in an increasingly large
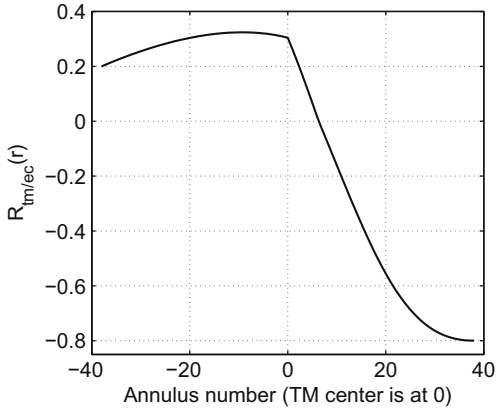

Fig. 2. Tympanic membrane reflection coefficient for a discretized membrane with 39 annuli, i.e., 77 samples. Note the asymmetry in $\mathscr{R}_{tm/ec}$. For the upper part of the TM ($N > 0$), $\mathscr{R}_{tm/ec}$ starts around 0.2 and slightly rises to 0.3 at the TM center ($N = 0$). As the canal cross-section area gets smaller and smaller, the impedance in the canal increases and the reflection coefficient decreases significantly. $\mathscr{R}_{tm/ec}$ is zero at $N = 7$, then negative.

characteristic impedance. The resulting reflection coefficient is shown in Fig. 2, for $N = 39$ annuli. Its non-symmetrical shape is determined by the combined influence of the TM impedance, symmetrically increasing from the periphery to the center, and the canal impedance, linearly increasing towards its termination. At the TM upper tip, the canal area is large and the reflection coefficient is 0.2 (it is greater than 0 to simulate a slight impedance mismatch). It then slightly rises to 0.3 at $N = -10$, remaining constant to the TM center, at $N = 0$. From this position, the TM impedance begins to decrease, as the canal impedance still increases (inversely as the area), resulting in a smaller reflection coefficient. It crosses zero at $N = 7$ and is negative for the remaining sections of the TM lower part $N > 7$.

At the canal termination, the canal area tends to 0, resulting in an impedance tending to infinity and a reflection coefficient tending to -1. Preliminary simulations have revealed that such large reflections are probably inappropriate. As a consequence, we have slightly decreased the negative reflection coefficients (in absolute value), corresponding to the canal termination. In practice, this has been done by scaling the negative values by 0.8.

The interface between the canal and TM wave models is summarized in Fig. 3. This is one of the key points of the model. The idea is that the single canal transmission line feeds several lines (two per annulus, except for the center) on the TM. The last canal sample is split onto the different delay lines, according to the ratio of the annuli areas over the entire TM area, then propagated along a portion of air corresponding to the remaining canal space, before hitting the TM (see Fig. 1a). At this point the lines meet the junc-
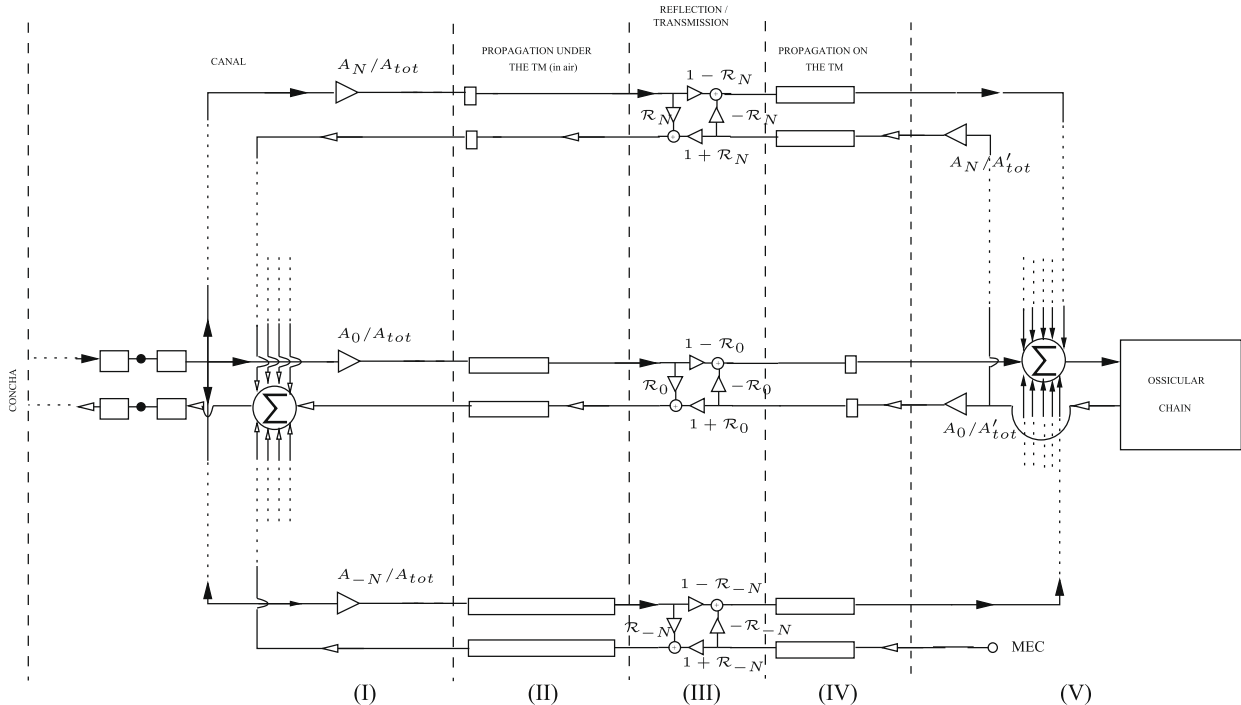

Fig. 3. Interface between the ear canal and the tympanic membrane. Forward and backward propagation path are represented by solid and hollow arrow heads, respectively. Rectangles represent transmission lines delays with length proportional to delay. In the first section from the left (Section I), at the canal termination, the last forward sample is multiplexed into the interface transmission lines and scaled according to the ratio of the stripe area A_i over the total TM surface area A_{tot}. The second section (Section II) represents transmission lines showing the wave in air under the TM; due to the inclination of the drum, they bring different delays. At the interface between the canal (air) and the membrane (Section III), the wave is split into a transmitted and a reflected part, computed from the knowledge of the reflection coefficient on the TM (see Fig. 2). In the Section IV the transmitted part propagates on the TM toward the umbo (rightmost series of transmission lines) where finally, in Section V, all contributions are added and then feed the OC. The reflected part at the canal/TM interface propagates in air back to the canal input. In the backward propagation, the wave coming from the OC is only input into the TM superior region, where it is in contact with the manubrium, and is multiplexed and scaled according to the ratio of the stripes areas over the superior region area, A'_{tot}. It propagates to the canal input using the same path than the forward-going wave. All contributions are then added before being input into the canal transmission line. Note that our actual implementation takes into account the future possibility of adding an input from the middle ear cavity space into the inferior region, but these (velocity) inputs are presently zeroed (far lower-right corner, labeled MEC).

tion with the TM and reflected and transmitted parts are computed from the function in Fig. 2: the reflected part is input into the backward-going transmission line corresponding to the same annulus, the transmitted part propagates on the TM towards the umbo. The volume velocity contributions from all the annuli are summed up at the umbo before being output to the OC model.

2.3. Ossicular chain model

The OC encloses the three ossicles – malleus, incus, and stapes – and propagates the sound wave from the TM, at the umbo, to the cochlea. The mechanical interactions between the three ossicles result in a lever ratio on the velocity and impedance (Guinan and Peake, 1967; Puria and Allen, 1998). The OC is not modeled as a pure delay line, as has been done for the TM or the canal, because it is a lumped structure, thus cannot be appropriately represented directly as a transmission line; in fact, it is well known that its components could be considered, like filters, as altering the wave in a frequency-dependent way. We have thus chosen to use a more conventional representation, the lumped-parameter circuit from Puria and Allen (1998), and O'Connor and Puria (2008). It has been slightly modified for our purpose and especially, it has been implemented in the time domain, so to be connected to the TM model.

Our lumped-parameter model for the OC is shown in Fig. 4. Note that it is slightly different from the one we used in (Parent and Allen, 2007):

1. the attic ligaments are now combined with the malleus in a single two-port,
2. the transformer modeling the OC lever ratio is brought to the left of the malleus,
3. the stapes is separated from the cochlea using the model by Lynch et al. (1982), and is implemented as its own two-port, to enable a more detailed access to its velocity.

The malleus, incus, and stapes are represented by 2-ports, which compute the forward and backward outputs from their forward and backward inputs. The malleus 2-port includes the bone itself, as well as the attic ligaments, and a shunt compliance, modelling the incudo-malleolar joint. The incus 2-port is simpler and includes the bone mass and the incudo-stapedial joint. The two bones are associated with a stiffness representing the joint: this stiffness is computed from the mass and the characteristic impedance to assure the "matched-impedance" condition (Puria and Allen, 1998); i.e., the stiffness is adjusted so that the mass/stiffness association generates no reflection. The stapes 2-port includes the stapes, as well as the annular ligament stiffness and its associated resistance. The final load is the cochlea, modeled by a 1-port.

Each 2-port can be described by a symmetric series impedance $Z/2$ and a shunt admittance Y, which are frequency-dependent. Using subscript "1" to denote quantities on the left-hand side of the 2-port and "2" for the right-hand side, we can write Kirchoff's laws in the frequency domain in terms of pressure and velocity as the following matrix equation:

$$\begin{bmatrix} p_1 \\ u_1 \end{bmatrix} = \begin{bmatrix} 1 + \frac{YZ}{2} & \frac{YZ^2}{4} + Z \\ Y & \frac{YZ}{2} + 1 \end{bmatrix} \begin{bmatrix} p_2 \\ u_2 \end{bmatrix}. \tag{4}$$

Introducing the medium characteristic impedance z_0, and decomposing pressure and velocity into forward and backward components, we also have on each side

$$p_i = z_0(u_i^+ + u_i^-), \tag{5}$$
$$u_i = u_i^+ - u_i^-. \tag{6}$$

Substituting Eqs. (5) and (6) into Eq. (4), we obtain a matrix equation involving the volume velocity components, z_0, and the 2-port elements, Y and Z as

$$\begin{bmatrix} u_2^+ \\ u_1^- \end{bmatrix} = \begin{bmatrix} T_{11} & T_{12} \\ T_{21} & T_{22} \end{bmatrix} \begin{bmatrix} u_1^+ \\ u_2^- \end{bmatrix}, \tag{7}$$
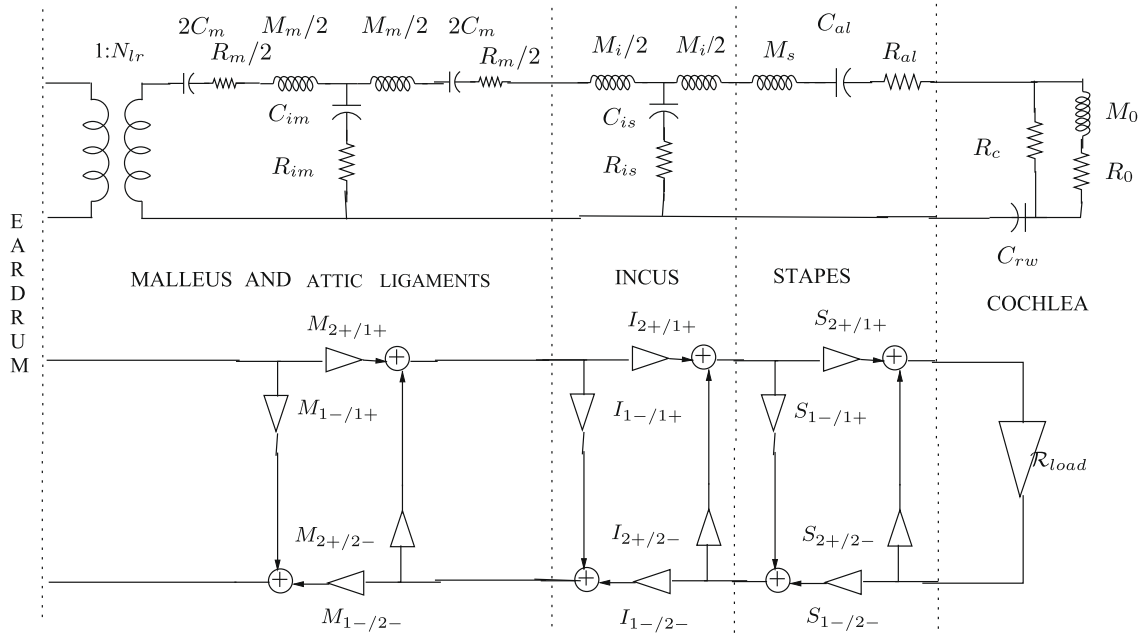

Fig. 4. Ossicular chain circuit representation. Each element is modeled by a 2-port with 4 filters given by the matrix of Eq. (7). The multipliers are frequency-dependent, and thus must be implemented as convolutions in the time-domain. $X_{2+/2-}$ represents the filter computing the forward output from the backward input, $X_{1-/1+}$ the backward output from the forward input, etc. The cochlear driving point impedance is modeled after Lynch et al. (1982). The OC lever ratio is represented by the transformer at the TM output, its ratio denoted N_{lr}. Malleus characteristic impedance is matched with the TM central impedance brought to the right-hand side of the transformer, i.e., multiplied by N_{lr}^2.

where the T_{ij} are fractions of polynomials in s, the Laplace variable. Each output is then a combination of the two inputs, filtered by a specific structure. Those filters are implemented in the time domain using the bilinear transform, and of course by keeping track of each filter's internal state variables.

Our model parameters are shown in Table 1, and compared to the values used by O'Connor and Puria (2008) (further denoted OP08), when fitting their model to the mean of 16 measurements on human temporal bones, coming from two different sessions. Overall, both models are in close agreement, except:

- incudo-stapedial joint compliance: our model joint is much stiffer, by a factor around 135. Our hypothesis, inspired from Puria and Allen (1998), is to treat the incus as a matched piece of transmission line, hence computing its joint stiffness from its mass so that its characteristic impedance would be matched to the OC. This approach has not been used by OP08, with each of their elements being adjusted separately,
- stapes and annular ligament: our model stapes mass is around 20 times larger and our annular ligament compliance 20 times smaller. The product mass × compliance, commonly appearing in our filters coefficients, will remain unchanged, but since the ratio is different, the propagation is significantly altered (see Eqs. (1) and (3)).

These differences are discussed further, in Section 4.1.

3. Results

3.1. Normal ear

3.1.1. Average fit

In this section, we show the results of our model simulations compared to experimental data, and we discuss the model performance. We also detail the interpretation of reflectance data in a more general manner (Voss and Allen, 1994; Feeney et al., 2003; Allen et al., 2005; Hunter et al., 2008; Withnell et al., 2009).

Simulations for the normal ear are shown in Fig. 5 where they are compared to the reflectance measurements of Voss and Allen

Table 1
Ossicular chain parameters values for our model, compared to the values reported by O'Connor and Puria (2008), in the case of their fit to the mean of two measurement sessions on human temporal bones (CGS units). Our values for the malleus two-ports have been corrected by the lever ratio for proper comparison.

Parameter	Value	O'Connor and Puria (2008), "AB"
TM characteristic impedance [g/(cm^{4}s)]	161.75–808.77	1050
TM area [cm^2]	0.6	0.6
Malleus mass [g]	2.3×10^{-3}	3.24×10^{-3}
Attic ligaments compliance [s^2/g]	1.67×10^{-6}	1.98×10^{-6}
Attic ligaments resistance [g/s]	150	140
Ossicles lever ratio	2	1.3
Incudo-malleolar joint compliance [s^2/g]	2.68×10^{-8}	6.85×10^{-7}
Incudo-malleolar joint resistance [g/s]	18.75	45.6
Incus mass [g]	9.98×10^{-4}	7.30×10^{-3}
Incudo-stapedial joint compliance [s^2/g]	7.36×10^{-10}	1×10^{-7}
Incudo-stapedial joint resistance [g/s]	75	30.4
Stapes footplate area [cm^2]	3.20×10^{-2}	3.14×10^{-2}
Stapes mass [g/cm^4]	63.51	3.55
Series annular ligament + round window compliance [cm^{4}s^2/g]	5.13×10^{-11}	9.01×10^{-10}
Series annular ligament + round window resistance [g/(cm^{4}s)]	1.50×10^6	2.99×10^5

(1994). This particular dataset has been chosen because it is readily available to the authors, and is widely recognized as a representative of normal human ears. Overall, the model is in good agreement with the experimental data. The detailed, rapid variations of the measurements are absent from the model, but the essential behavior is captured in some detail. The power transmittance, $T = 10\log_{10}(1 - |\mathcal{R}|^2)$, shown in Fig. 5a, gives a useful summary of the ear behavior: since it is on a decibels scale, the transmittance is closely related (though not equal) to the middle ear transfer function, hence its clinical advantage for hearing diagnosis (Allen et al., 2005). The middle ear system roughly acts as a band-pass filter, energy being reflected below about 1 kHz due to the stiffness components, and above 5 kHz due to the mass components. This behavior is consistent across the different examples but ±2 dB variability appears at high frequencies, above 5 kHz. The pressure reflectance magnitude plot ($|\mathcal{R}|$), in Fig. 5b, shows the same behavior, from the point of view of the reflected ear canal pressure or velocity. Note how the reflectance magnitude shows more variability than the power transmittance: as $|\mathcal{R}|$ approaches zero, a large relative change $\delta\mathcal{R}/|\mathcal{R}|$ maps to a very small (much less than 1 dB) change in $1 - |\mathcal{R} + \delta\mathcal{R}|^2$.

The behavior of the ear can be divided into three main frequency regions: at low-frequencies, it is stiffness-dominated and the transmittance rolls off by 6 dB per octave ($|\mathcal{R}| \to 1$ as $f \to 0$); at high frequencies it usually becomes mass-dominated, so that in many normal ears, $|T|$ decreases by a few decibels between 5 and 8 kHz, usually to reach values between −10 and −5 dB ($|\mathcal{R}|$ is between 0.6 and 0.9). In the mid-frequency range (1–5 kHz), the ear is best matched with the canal and the transmittance is at its maximum, fairly stable around −2 or −3 dB (reflectance is at its minimum, usually between 0.4 and 0.6). This typical behavior is usually well represented in artificial ears, such as the B&K4157 (shown here), or the DB-100 (Voss and Allen, 1994). Note that the roll-off of the reflectance above 10 kHz may be more likely due to limitations of the ER-10C earphone used for the measurements, than to the impedance method and model. The main limitation of the model is that it does not capture this transition from the stiffness-dominated state to the mass-dominated state, where human data show that reflectance has more across ears variability with frequency.

The phase and group delay plots, in Fig. 5c and d, provide key information about middle ear wave propagation. First, in the case of a single major reflection on the eardrum, the phase is roughly linear with frequency; other phase behavior means that the sound has been reflected from another site, such as the stapes. The frequency where the reflectance phase crosses $-\pi$ (around 7 kHz in these examples) is where a canal standing wave occurs, as confirmed by the minimum in the normalized impedance magnitude, in Fig. 5e. Estimating and appreciating the position and magnitude of such a canal standing wave is critical in the understanding of the middle ear. These standing waves are the focus of several studies (Stinson et al., 1982; Neely and Gorga, 1998; Scheperle et al., 2008; Withnell et al., 2009), especially to applications of hearing aid fitting. The round-trip delay can also be evaluated from the phase slope, giving useful estimate of the residual canal length; however this method can be inaccurate; in fact, the group delay (the phase derivative) tends to be very noisy at high frequencies, but still gives a relevant canal length estimate (Voss and Allen, 1994). Note that group delay plots shown here (Fig. 5d) have been derived from a smoothed version of the phase (using an average filter) to reduce this variability.

Normalized impedance plots in Fig. 5e–h give useful information about the actual impedance elements present in the propagation path. The impedance phase plot, in Fig. 5f, summarizes the system behavior in a very concise way: it is stiffness-dominated below about 0.8 kHz, then transitions to a "matched" state at
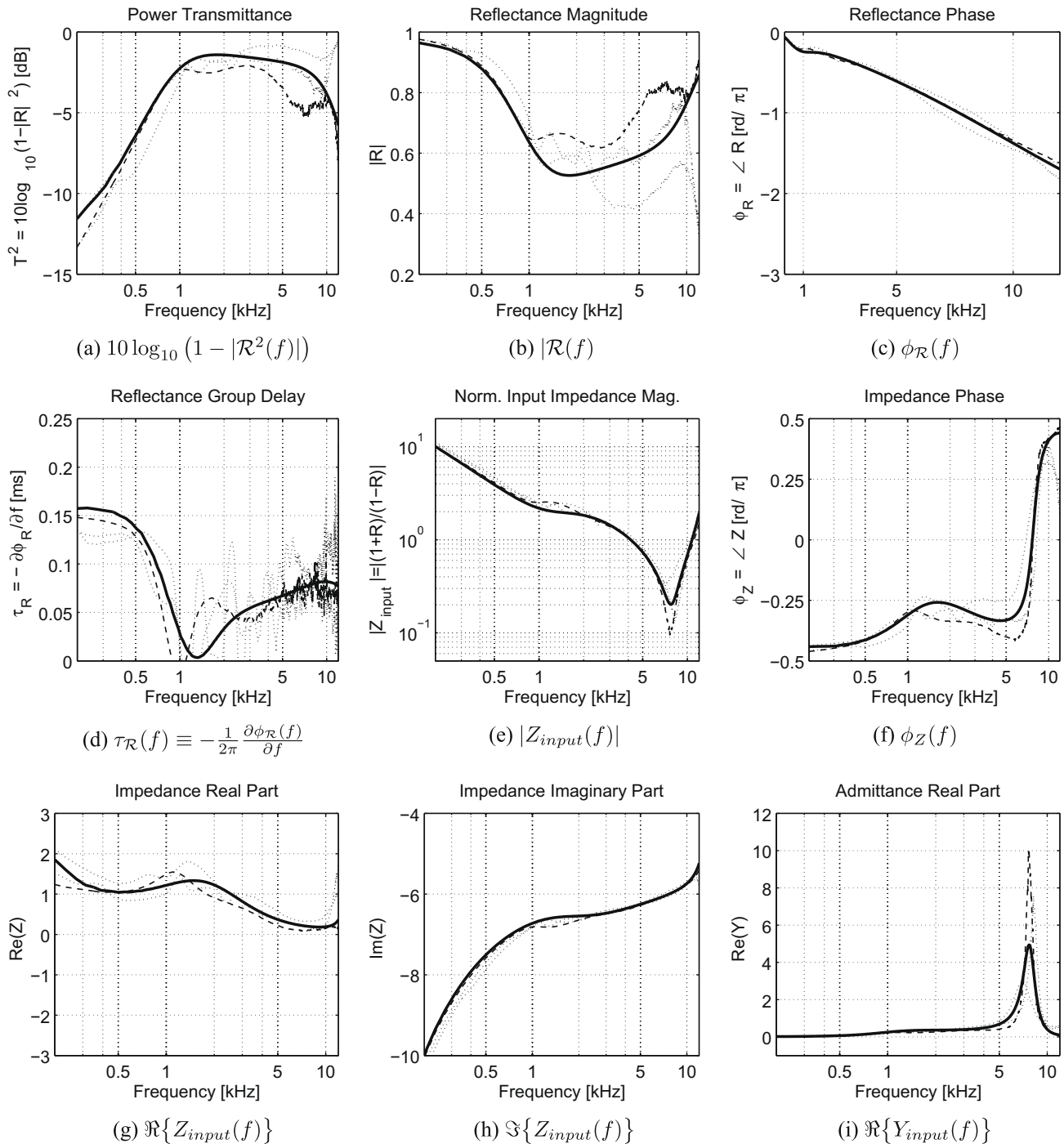
Fig. 5. In this figure we compare our model [solid] to several experimental examples from Voss and Allen (1994), for the normal ear: a typical subject [dash-dotted], the mean of all subjects [dotted], and the B&K4157 artificial ear [dashed]. Note that impedance plots refer to the normalized impedance, i.e., a dimensionless quantity. At low frequencies, the impedance phase (Fig. 5f) is close to $-\pi/2$, underlining the stiffness-dominated state, then remains around $-2\pi/3$ in the pass-band. The frequency where it crosses 0 indicates the standing wave in the canal, which for typical normal human ears, occurs above 6 kHz.

mid-frequencies, and then eventually can become mass-dominated in a limited frequency range around 10 kHz. The three experimental curves shown are typical of the normal human middle ear behavior; in particular, in the pass-band (1–6 kHz), the phase remains roughly between $-2\pi/3$ and $-\pi/4$, before sharply shifting to the mass-dominated state, approaching $+\pi/2$. The frequency at which the impedance phase crosses 0 is highly significant: the canal impedance has an anti-resonance there and it indicates the frequency (and hence the spatial position) where the standing wave (pressure and impedance minimum) occurs in the canal. This frequency varies from one individual ear to the next, essentially depending on their ear dimensions, but is typically above 6–7 kHz in young normal ears. This anti-resonant frequency directly correlates to the middle ear delay at high frequencies.

This transition, from stiffness to mass-dominated state, is typical of a closed transmission line, with the position of the first impedance minimum being related to the cavity length, defined by location of the TM. The real part of the normalized impedance

(the resistance) mainly results from the system characteristic impedance (from the input point of view) and is consequently usually around 1, the matched condition. Frictions in the middle ear, which further dissipate energy, tend to add frequency dependency below 0.3 kHz, and around 2 kHz in Fig. 5g.

The admittance (reciprocal of the impedance) real part, shown in Fig. 5i, shows a large localized peak where the impedance is minimal, corresponding to the frequency of the ear canal standing wave. The estimation of this important frequency has implications and applications to clinical diagnosis, especially for in-the-ear calibration protocols (Withnell et al., 2009).

Delays can be easily estimated by a regression of reflectance phase with frequency. We have estimated delays in the propagation path by looking at the phase shift of the forward wave and we conclude that:

- TM one-way delay: 24 μs,
- OC one-way delay: 9 μs.

Note these delays are different from the ones usually computed from the total pressure or velocity, including both forward and reflected waves. Estimating the delay from the forward path estimates the actual physical delay. The total pressure estimate can be quite different.

3.1.2. Individual fits

In the previous section, we have verified that the model was able to capture the average behavior of the human ear. In this section, we try to fit the model to individual data, measured by Voss and Allen (1994). The subjects shown here have been randomly selected, with no *a priori* knowledge of their impedance behavior. The results of our individual fits are shown on Figs. 6–8. Adjusting the model parameters to best fit a specific dataset can be a very time-consuming and tedious process. However, it is generally pos-

sible to achieve a reasonable – though, less accurate – fit with limited adjustments. This is the approach we have followed in this section. It is quite clear that the model is too simple to deal with the subtle variations of each subject, but we are indeed able to adjust it to follow the overall trends.

Below are briefly summarized the specificities of each subject (compared to the average case), from our model point of view:

- Subject 3: increased ossicles mass,
- Subject 9: decreased ossicles mass, increased stiffness,
- Subject 10: reduced ear dimensions, increased stiffness, and stapes mass.

3.2. Otosclerosis

The term "otosclerosis" means "abnormal bone growth in the middle ear", but is used clinically to describe the fixation of the stapes footplate to the oval window of the cochlea, due to an abnormal growth of the bone. Any such stapes fixation greatly impairs movement of the stapes, and therefore transmission of sound into the inner ear. Additionally, the cochlea round window can also become sclerotic, and in a similar way impair movement of sound pressure waves. From our model point of view, this pathology is modeled by the increase of the stapes mass and of the annular ligament joint stiffness. We have defined an otosclerosis variable (factor), denoted *otoscl* ($otoscl = 2$, in our simulations), and performed the following transformations:

- stapes mass: $M_s \mapsto M_s \times otoscl^{1.7}$,
- annular ligament stiffness: $K_{al} \mapsto K_{al} \times otoscl^{1.6}$.

Furthermore, the canal length was increased to 7 mm, due to a different insertion depth in these measurements. The values for

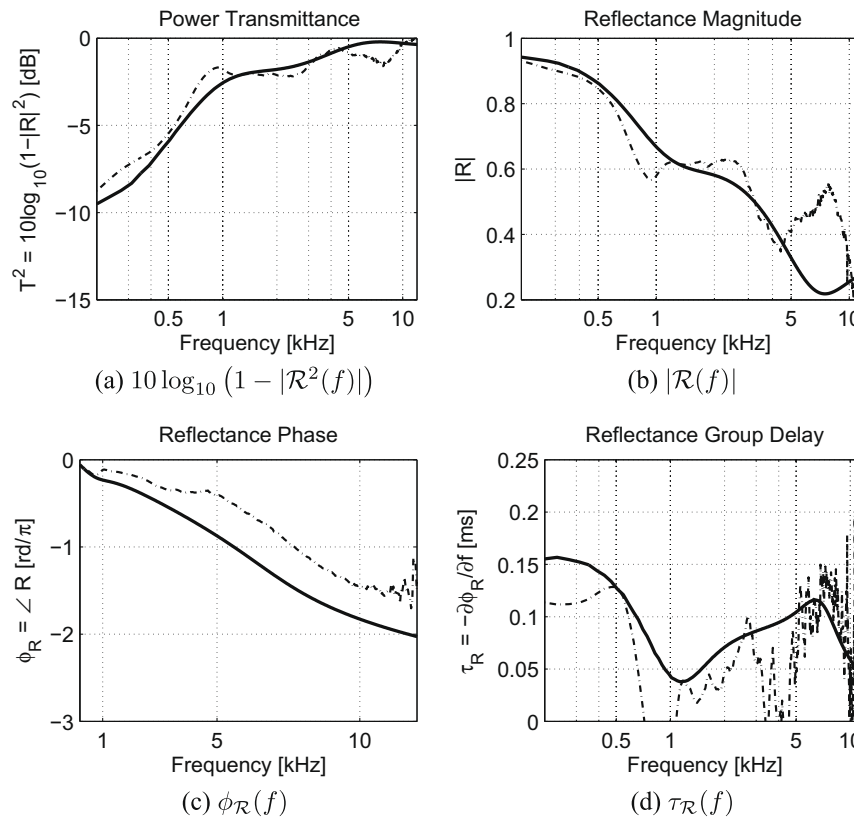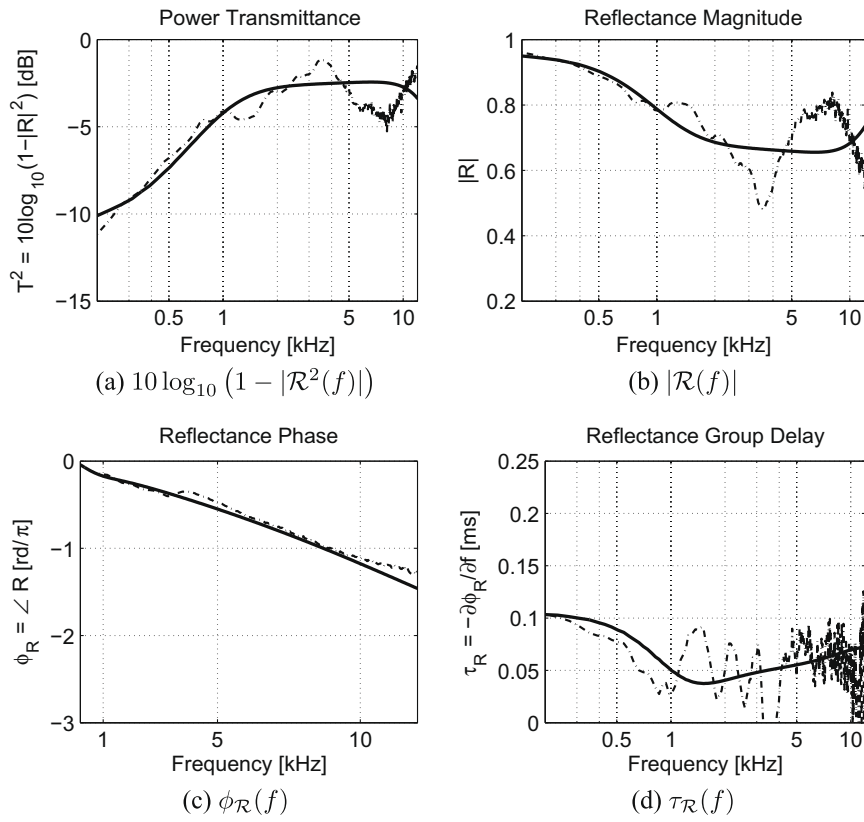**Fig. 6.** Model (solid line) fitted to subject 3 from Voss and Allen (1994) (dash-dotted).

(a) $10 \log_{10} \left(1 - |\mathcal{R}^2(f)|\right)$

(b) $|\mathcal{R}(f)|$

(c) $\phi_{\mathcal{R}}(f)$

(d) $\tau_{\mathcal{R}}(f)$

Fig. 7. Model (solid line) fitted to subject 9 from Voss and Allen (1994) (dash-dotted).

(a) $10 \log_{10} \left(1 - |\mathcal{R}^2(f)|\right)$

(b) $|\mathcal{R}(f)|$

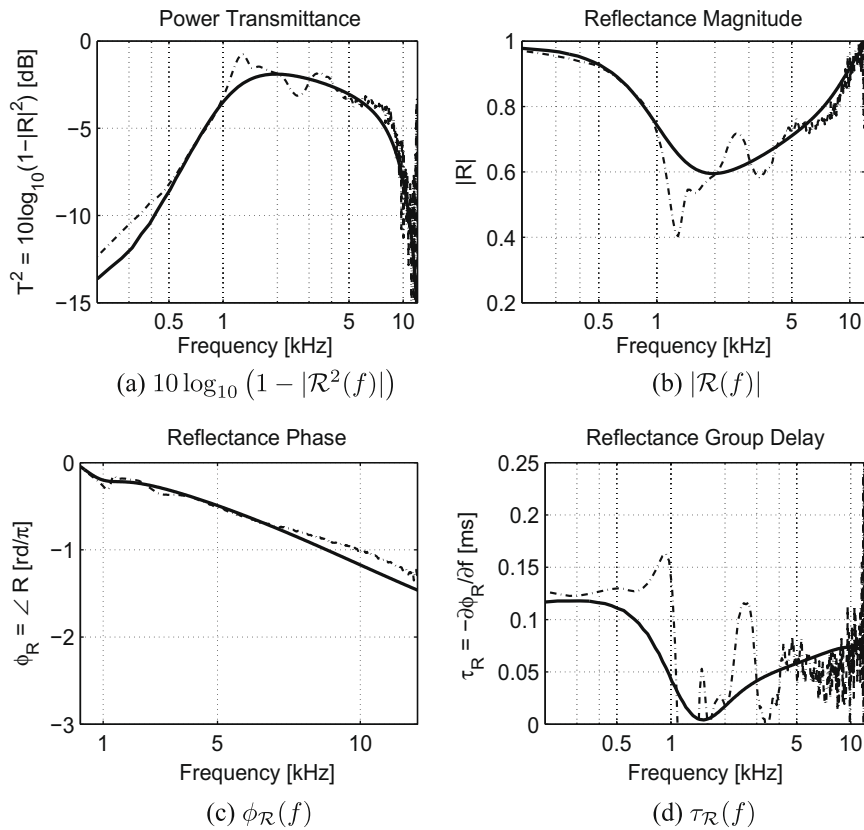(c) $\phi_{\mathcal{R}}(f)$

(d) $\tau_{\mathcal{R}}(f)$

Fig. 8. Model (solid line) fitted to subject 10 from Voss and Allen (1994) (dash-dotted).

otoscl and its exponents have been empirically derived, with the intention to best fit experimental data. The use of a single parameter ensures that the various contributions are varied systematically. Note that the combination of parameter values to obtain such results may not be unique, but the one we detail here has been derived through our physical insight of the ear impedance, and consequently makes physical sense. The consequences of otosclerosis are mainly seen at low frequencies, where the stiffness-dominated region has a wider bandwidth, with a transition to the matched state shifted to higher frequencies. The model predictions for this case are shown in Fig. 9. The high-frequency limitations of the model previously mentioned are more obvious here, especially in the reflectance plot, in Fig. 9b, as the solid line; in fact, the model directly transitions from the stiffness-dominated state to the mass-dominated state, and the reflectance increases significantly above 2 kHz. This is obviously different from real otosclerotic ears which have a behavior quite similar to a normal ear above 2 kHz, with a smaller reflectance magnitude. It seems clear that some structure is missing in the model which would play a critical role in the otosclerotic ear between 3 and 5 kHz. However, the general behavior is still well captured by the model, as can be seen from the other plots in Fig. 9. It could simply be that the model parameters need further refinement.

3.3. Otitis media with effusion

Otitis media results from an inflammation of the Eustachian tube, typically in infants. The tube then no longer equalizes the pressure in the middle ear and throat, which results in fluid flowing back to the middle ear cavity and constraining significantly the TM and OC movements, depending on the seriousness of the pathology. Physically, this results in the system being much stiffer and lossy (more friction). In our model, this is represented by a parameter *ome* (*ome* = 7, in our simulations), and the following parameters changes:

- middle ear characteristic impedance: $z_{me} \mapsto z_{me} \times ome$,
- malleus and incus mass: $M_{m,i} \mapsto M_{m,i} \times ome^{1.2}$,
- incudo-malleolar and incudo-stapedial joints stiffness: $K_{im,is} \mapsto K_{im,is} \times ome^{1.3}$,
- stapes mass: $M_s \mapsto M_s \times ome^{1.2}$,
- annular ligament stiffness: $K_{al} \mapsto K_{al} \times ome^{1.4}$,
- annular ligament resistance: $R_{al} \mapsto R_{al} \times ome^{0.5}$.

Here the residual canal length is 1 mm. Obviously the model modifications are extensive. As for the otosclerosis example, the values for *ome* and its various exponents have been manually adjusted to match experimental data, and the resulting combination may not be unique. The use of a single parameter, *ome*, ensures consistency among all affected parameters, but at the same time is limiting.

The resulting predictions are shown in Fig. 10, and compared to experimental data measured in two infants (Gravel, 1999–2002). From the reflectance magnitude point of view, the behavior is quite similar to otosclerosis, with an increased stiffness shifting the first resonance to higher frequencies. The matched band is even more restricted. The main difference with otosclerosis resides in the phase, and thus group delay; in fact, we observe a major disruption around 3 kHz, probably due to a secondary reflection site from the stapes. The round-trip delay is also much greater at that frequency (425 μs vs. less than 100 μs in the sclerotic ear), suggesting that energy is trapped between two reflection sites, and thus not been transmitted into the cochlea. The model results are in agreement with experimental measurements but, again, we can underline
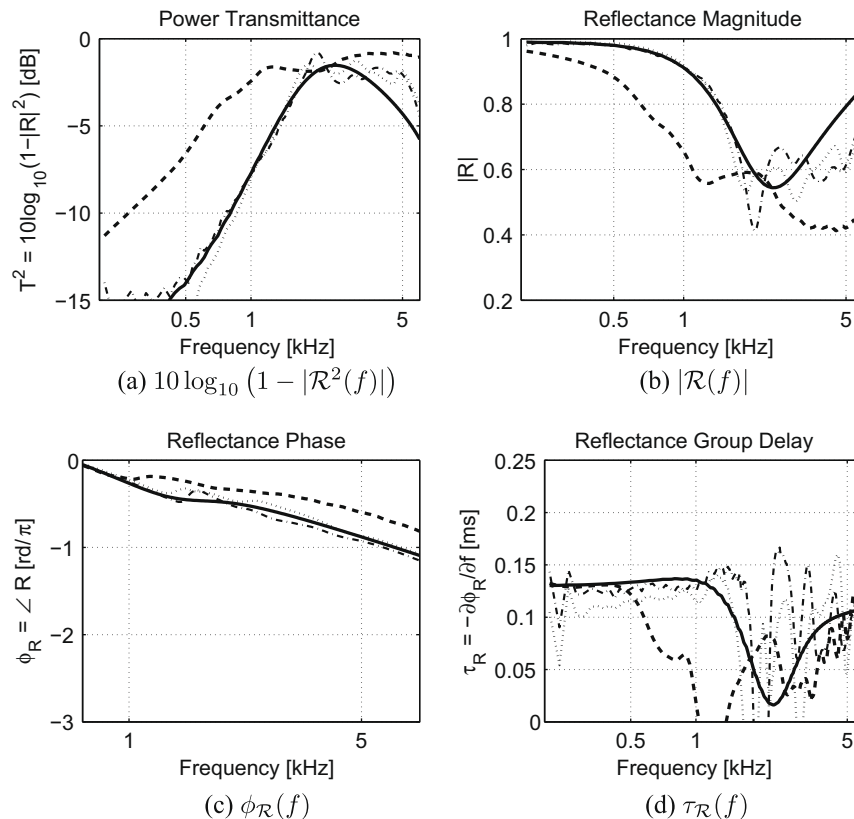

(a) $10\log_{10}\left(1 - |\mathcal{R}^2(f)|\right)$ (b) $|\mathcal{R}(f)|$

(c) $\phi_{\mathcal{R}}(f)$ (d) $\tau_{\mathcal{R}}(f)$

Fig. 9. Model simulation for the otosclerotic ear (solid line). Experimental data has been collected on a human patient, up to 6 kHz (Allen et al., 2005). The left ear is shown in dash-dotted lines, and the right ear in dotted lines. The thick dashed line is the average normal ear from Fig. 5, for reference.
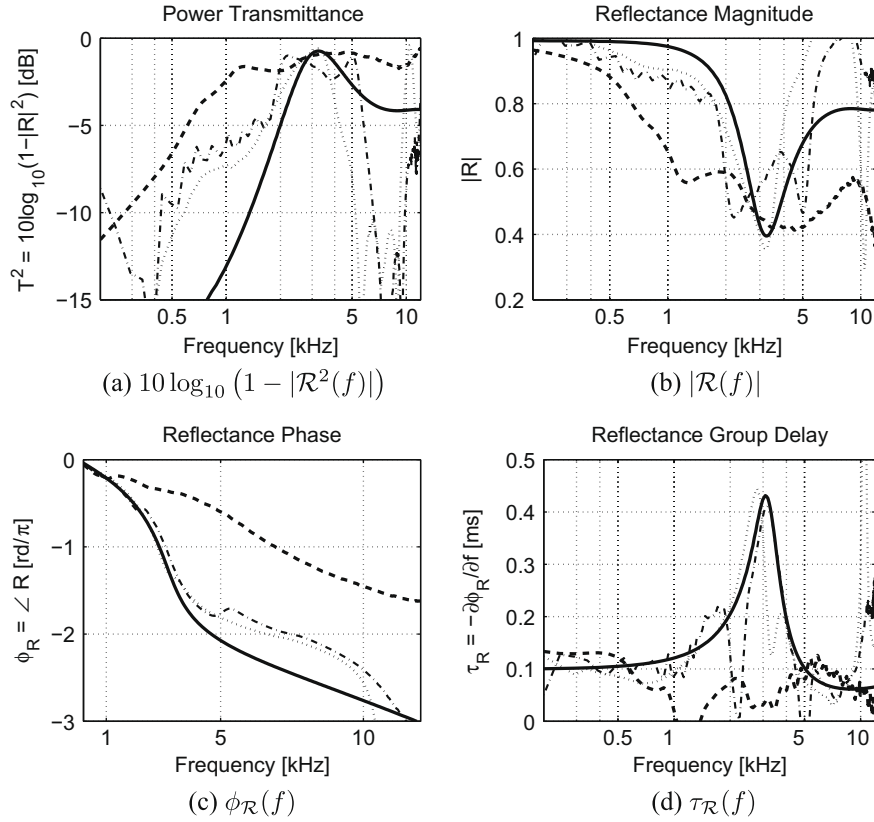
Power Transmittance

Reflectance Magnitude

Reflectance Phase

Reflectance Group Delay

Fig. 10. Model simulation for the ear with otitis media with effusion (solid line). Two typical human ears with otitis media are represented in dash-dotted and dotted lines. The thick dashed line is the average normal ear from Fig. 5, for reference.

3.4. Impedance matrix

In order to further evaluate the behavior of the model, we compute its impedance matrix, defined as

$$\begin{bmatrix} p_{ec} \\ p_{st} \end{bmatrix} = \begin{bmatrix} Z_{11} & Z_{12} \\ Z_{21} & Z_{22} \end{bmatrix} \begin{bmatrix} u_{ec} \\ u_{st} \end{bmatrix}, \tag{8}$$

where p_{ec} and u_{ec} are the pressure and volume velocity at the canal input, and p_{st} and u_{st} their equivalents at the stapes. The impedance matrix elements are computed as follows:

$$Z_{11} = \left. \frac{p_{ec}}{u_{ec}} \right|_{u_{st}=0}, \tag{9}$$

$$Z_{12} = \left. -\frac{p_{ec}}{u_{st}} \right|_{u_{ec}=0}, \tag{10}$$

$$Z_{21} = \left. \frac{p_{st}}{u_{ec}} \right|_{u_{st}=0}, \tag{11}$$

$$Z_{22} = \left. -\frac{p_{st}}{u_{st}} \right|_{u_{ec}=0}. \tag{12}$$

Note the negative signs when the model is driven in reverse. These equations become even simpler in our case, where the input velocity is a unity pulse. For example, when driving the model from the canal, we get

$$Z_{11} = \left. \frac{p_{ec}}{1} \right|_{u_{st}=0} = p_{ec}|_{u_{st}=0}, \tag{13}$$

$$Z_{21} = \left. \frac{p_{st}}{1} \right|_{u_{st}=0} = p_{st}|_{u_{st}=0}. \tag{14}$$

The equations are very easily implemented in our wave model because they merely correspond to a one-line modification of the code at each termination of the transmission line. Alternatively, the corresponding admittance matrix can be computed by changing the boundary conditions so that the input pressure is a unity pulse and the total pressure at the other termination is null.

In practice, we set a total reflection on each side (reflection coefficient of 1, so that the total volume velocity is 0) and input a single velocity pulse at each termination, depending on the tested condition. We have computed the impedance and admittance matrices at different locations along the OC and realized that the model is very sensitive to these specific boundary conditions, characteristic of a low-loss delay network; in fact, we had to slightly increase the attenuation factor (see Section 2.1) to 0.3% so that the simulation did not diverge. Note that this damping does not correspond to a specific physical element of the propagation path, rather to the medium thermal and viscous losses; mathematically, those would correspond to a non-zero real part of the propagation factor (see Eq. (1)) (Keefe, 1984). Besides, without this added loss, some computations would output non-physical driving-point impedances (Z_{11} or Z_{22} phase outside $[-\pi/2; +\pi/2]$ radians at poles or zeros), while the admittance would be physical, or vice-versa. A tentative explanation for this instability is described further.

We have compensated for the various transformer ratios along the OC, and we have computed normalized impedances, i.e., the pressure is the sum of the velocity components, and is not multiplied by the local characteristic impedance. This removes the dif-

ferent impedance transformations, simplifying comparisons between the two boundary conditions.

The elements of the impedance matrix computed between the canal input and the stapes are shown in Fig. 11. The low-frequency gain of the impedance is the TM transformer ratio, i.e., $30/N_{tr}^2$ (see Section 2.2). The two driving-point impedances (when the pressure and velocity are measured at input), Z_{11} and Z_{22}, are indeed characteristic of a closed transmission line, as could be expected. The two transfer impedances, Z_{12} and Z_{21}, are more difficult to appreciate: they are not driving-point impedances, since their pressure and velocity are measured at different locations, resulting in their phase being outside $[-\pi/2; +\pi/2]$ radians, due to the propagation delay between the two locations. Their responses are similar in trend, but they differ noticeably between 2 and 12 kHz. The difference is, at most, 0.7 dB in magnitude (8% error), and 0.2π radians in phase (30% error).

These errors reveal that the model is not perfectly reciprocal, and underline a limitation of our current implementation. Further investigation revealed that time-domain artifacts could be the source of the model instability in these specific boundary conditions, and also explain its non-reciprocity. More precisely, we have verified that the "non-reciprocal" behavior of the model was brought by the TM. These time artifacts are a direct consequence of our implementation and of the fact that the TM delays, as being necessarily multiples of the sampling period, are not perfectly aligned, resulting in a slight desynchronization of the different lines (see Parent and Allen (2007), Fig. 6). This could be fixed, for example by using all-pass filters before summing the different contributions, to align the delays; however, we have not pursued this possibility here.

3.5. First conclusions

In general, the model is in agreement with experimental data. The match is very good with average normal data, but is poorer as the response complexity increases, typically for individual data, or pathological ears. Modifying the model parameters in a physical manner to follow the different behaviors does alter the model results in a predictable way.

The impedance matrix computed from the model is also physical and corresponds to our intuitive understanding of the propagation. The computation of the transfer impedances reveals that the TM introduces a slight non-reciprocal behavior, possibly due to the quantization of the TM delays. We argue that while this inaccuracy requires careful investigation, it does not invalidate the modeling approach, i.e., to represent the TM by a combination of delay lines;

in fact, a more sophisticated implementation of these delays is likely to improve the model behavior.

Those are promising results: eventually, with a more sophisticated model, we hope to be able to more accurately simulate individual data and refine our interpretation of pathologies. Also, we believe that the ability to discriminate between the forward and backward components of the sound wave, and the consequent ability to estimate forward and backward delays, can be very helpful in providing understanding to on-going work aimed at isolating the forward wave reflected from the eardrum.

These results confirm the relevance of our distributed model of the TM. We have deliberately chosen to simplify it, and focus on the wave propagation pattern. The extent to which we match experimental data demonstrates that the TM acts as a transmission line. More specifically, it suggests that complex motion and multi-moding of the eardrum may not be critical to the general wave propagation. Rather it is the impedance matching horn properties of the TM that are the most important. These necessarily introduce delay.

3.6. Validation with independent data

In order to further validate the model, we now compare it to data which have not been used in its derivation. Here, we use temporal bones results published by OP08, with their frequency-domain model. Their model uses a very similar lumped-parameter circuit for the ossicular chain to ours, coupled to a delay line representing the TM. Their parameters are adjusted to fit transfer functions measured on human temporal bones, collected during different measurement sessions, and then separated in ensembles A ((O'Connor and Puria, 2006), 4 bones) and B ((O'Connor et al., 2008), 12 bones). Their model is adjusted to fit each individual measurement, plus the mean of all 16 bones (denoted "AB"). For the comparisons shown in this section, our model parameters have not been modified, but are the ones from the normal ear case. In the following figures, for each dataset (A and B), we show the mean of all measurements in dotted line and the mean of the corresponding fitted models in dashed line with our model the solid line.

3.6.1. Middle-ear transfer function

Fig. 12 shows the middle ear transfer function, computed as the ratio of the stapes velocity to the canal pressure at the eardrum. The model from OP08 has been fitted to those measurements and consequently matches the experimental data very well. Note how the transfer function magnitude rolls off above 1 kHz as the
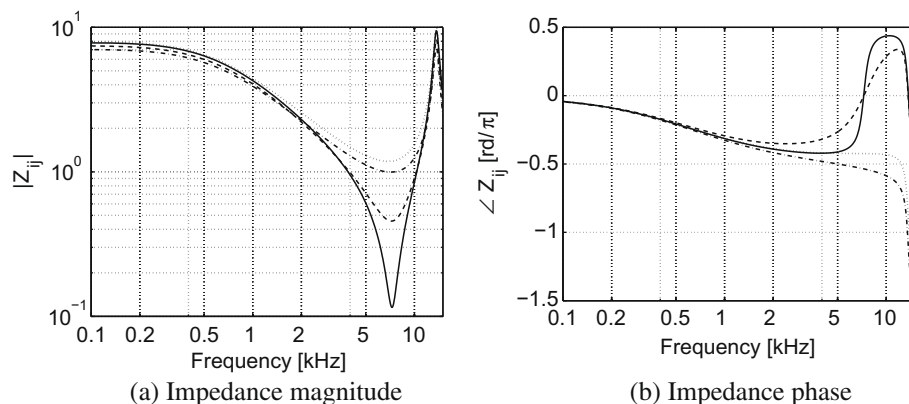

(a) Impedance magnitude
(b) Impedance phase

Fig. 11. Impedance matrix for the middle ear model, between the canal and the stapes. The impedance magnitude is shown on the left, the phase on the right. In both plots, the two driving-point impedances, Z_{11} and Z_{22}, are shown in solid and dashed lines, respectively. The transfer impedances, Z_{12} and Z_{21}, are shown in dotted and dash-dotted lines, respectively.
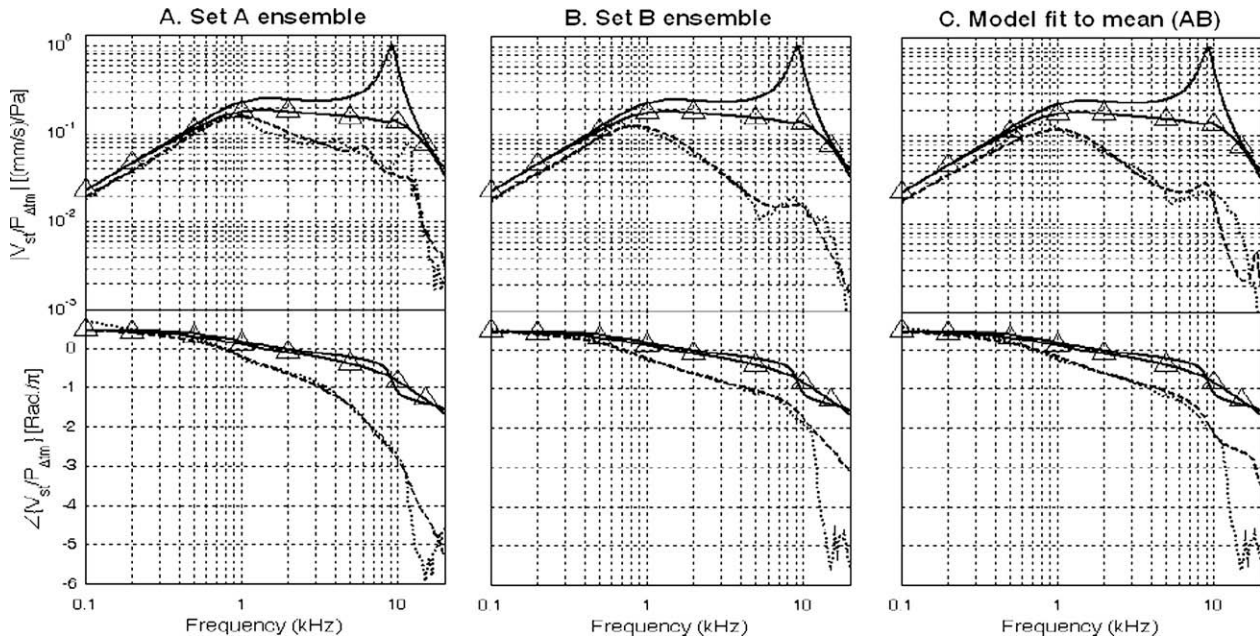
Fig. 12. Our model compared to data and model simulations from OP08: ratio of the stapes footplate velocity over the canal pressure at the eardrum, magnitude (top row) and phase (bottom row). For each data set (A and B), mean experimental data is shown in dotted line, and mean model simulation by OP08 in dashed line. Our model is shown as the solid line, uncorrected (no markers) and corrected by $(1 + \mathcal{R})/2$ (upwards triangles). The third column represent the OP08 model fit to the mean measurement from sets A and B.

reciprocal of the frequency (−6 dB per octave). This behavior is consistent with previously-published temporal bones data (Aibara et al., 2001) and living ears (Huber et al., 2001) but is, however, quite surprising since it does not correspond to our intuitive understanding of the middle ear, which would be expected to have a flat response between 1 and 4–5 kHz, as is typically seen in hearing thresholds (Fletcher and Munson, 1933).

Our model (solid line) is in agreement with OP08 responses below 1 kHz, except for a 2 dB gain difference; this is due to our ossicles lever ratio being slightly larger. However, above this frequency, our transfer function remains flat up to 5 kHz, where it again starts to rise, reaching a resonance peak at 9 kHz, before sharply rolling off above 10 kHz. The 9 kHz resonance is due to a corresponding minimum in the canal pressure, created by the interaction of forward and backward waves in the canal, i.e., the well-known canal standing wave. The degree of peaking depends directly on $|\mathcal{R}|$ at that frequency, as discussed in Section 3.1.1 and Fig. 5. A null in the pressure corresponds to a peak in the transfer function (at 7 kHz in Fig. 5e). Note that our model transfer function is very similar in shape to the ear input admittance magnitude (Fig. 5i). This is because both have a common $1/(1 + \mathcal{R})$ factor:

$$Y = \frac{1}{z_0} \frac{1 - \mathcal{R}}{1 + \mathcal{R}}, \qquad (15)$$

$$\frac{V_{stapes}}{P_{canal}} = \frac{V_{stapes}}{P_{canal}^+ + P_{canal}^-} = \frac{V_{stapes}}{P_{canal}^+(1 + \mathcal{R})}, \qquad (16)$$

where P_{canal}^+ and P_{canal}^- are the forward and backward components of the canal pressure wave.

Following the method suggested by Withnell et al. (2009), we also display our model transfer function corrected by $(1 + \mathcal{R})/2$ (upwards triangles) which removes the standing wave effect and is more useful for interpretation. The data from OP08 does not show any major standing wave because the measurements have been averaged; as the effect is very measurement-specific, it disappears with the mean. For the same reason, we have not corrected these responses by $(1 + \mathcal{R})/2$ because only the mean reflectance was available to us.

The discrepancy is even more obvious in the phase plots, in the bottom row; in fact, our model shows a much smaller delay. The slope rupture at 9 kHz corresponds to the canal standing wave, and disappears with the corrected response. We have computed the group delay of our model transfer function, by linear regression of the corrected phase between 2 and 11.1 kHz (cf. OP08, page 209), which yielded a value of 43.6 μs, compared to means of 127.1 and 54.9 μs, for set A and set B, respectively (Table II in OP08). Possible reasons for these very large differences are discussed in Sections 3.6.3 and 4.2.

3.6.2. Ossicles velocities

The ratios of ossicles velocities are shown in Fig. 13. Looking at the magnitude plots (top row) for V_{st}/V_u (no markers) and V_i/V_u (upwards triangles), we observe a similar discrepancy between our model and that OP08; namely, above 1 kHz, their model and experimental data rolls off, while our model remains flat, up to 5 kHz. Still, the general behavior is rather well captured by our model. V_{st}/V_i rolls off at 5 kHz in the data, and at 17 kHz in our model.

The linear regression on the V_{st}/V_u phase between 2 and 11 kHz gives us an OC delay of 29.8 μs, while estimated at 51.6 μs in set A, and 37.5 μs in set B. Subtracting this delay from the one computed on the global transfer function in the previous section, we can estimate the TM delay at 12.1 μs. Estimates from OP08 gave 75.7 μs for set A, and 17.6 μs for set B. Note that this TM delay is computed using the total velocity, i.e., the difference between the forward and reflected waves; as a consequence, it results in a different delay estimate than the one using the sole forward wave, presented in Section 3.1.1.

3.6.3. Complex reflectance

The reflectance plots in Fig. 14 compare our model in solid line to measurements in dotted lines from Hudde (1983) (upwards triangles), Farmer-Fedor and Rabbitt (2002) (downwards triangles), and Voss and Allen (1994) (data not used to fit the model: a different subject from the one shown in Section 3.1.1 with square mark-
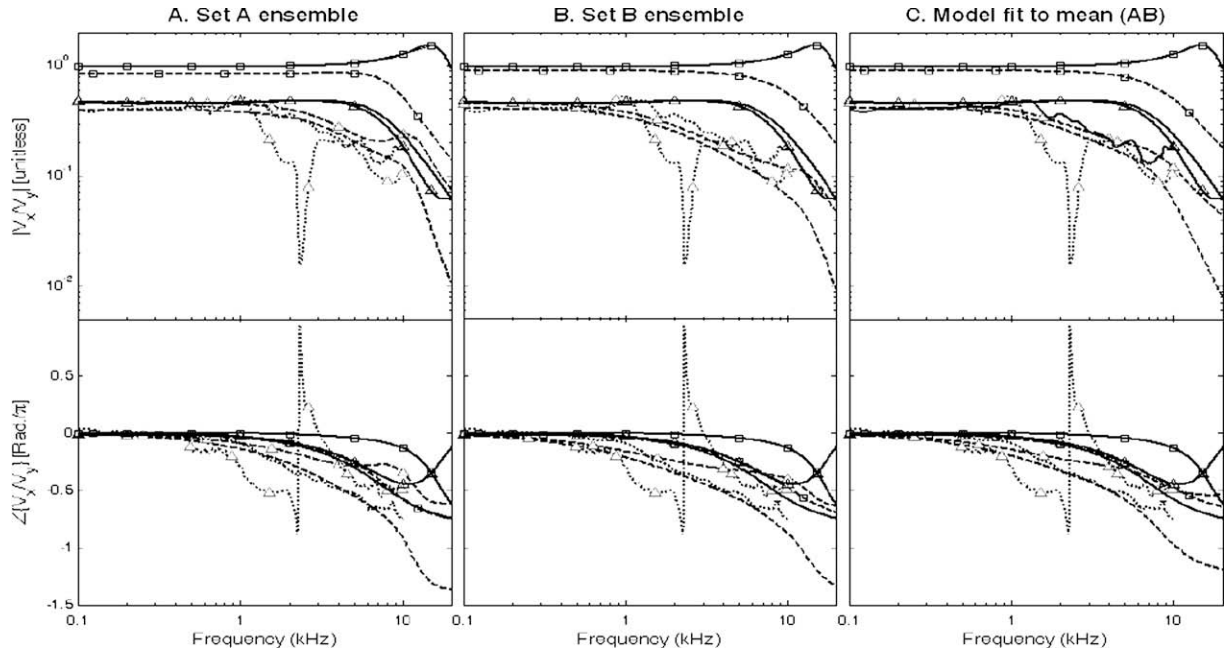
Fig. 13. Our model compared to data and model simulations from OP08: ratio of ossicles velocities, magnitude (top row) and phase (bottom row). Velocities at umbo, incus, and stapes are denoted V_u, V_i, and V_{st}, respectively. V_{st}/V_u is shown with no markers, V_i/V_u with upwards triangles, and V_{st}/V_i with squares. Our model is the solid line, model simulations from OP08 are the dashed lines, and their experimental data are the dotted lines. No experimental data is available for V_{st}/V_i. The third column represent their model fit to the mean measurement from sets A and B.
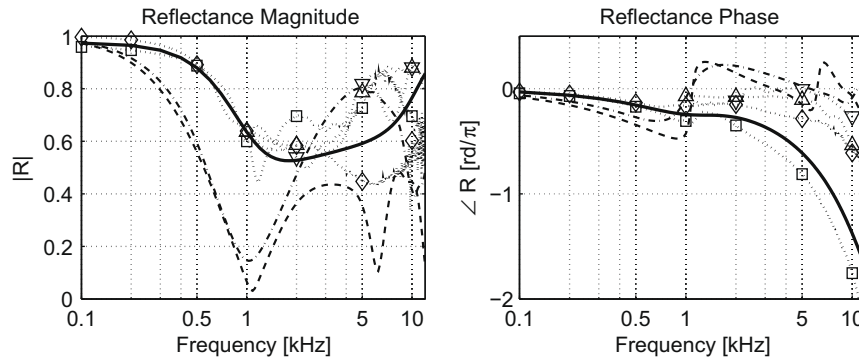

Fig. 14. Our model compared to model simulations from OP08 and other experimental data: reflectance, magnitude (left) and phase (right). Our model is the solid line, the model from OP08 fitted to dataset A is the dashed line, and their model fitted to dataset B is the dash-dotted line. Experimental data are in dotted line, with the upwards triangles (Hudde, 1983), downwards triangles (Farmer-Fedor and Rabbitt, 2002), and squares and diamonds another subject and the DB-100 coupler from Voss and Allen (1994), respectively. The model from OP08, fitted to middle ear transfer functions, shows clear oscillations above 1 kHz, which could point out to a delay error.

ers, and the DB-100 coupler with diamond markers), as well as the model from OP08 fitted to dataset A (dashed), and B (dash-dotted). We have dropped the data from Voss et al. (2000) published in OP08 because it had been corrected for the middle ear cavity impedance. The original OP08 paper reports these data as input impedance plots, but those are difficult to interpret due to the influence of the measurement probe placement, which $|\mathcal{R}|$ is insensitive to. The complex reflectance separates the impedance-mismatch effect in its magnitude, from the delay effect in its phase and is consequently more relevant. We have converted the MKS impedance data from OP08 using the same characteristic impedance for all those measurements (3.28×10^7 kg/m^{4}s, provided in their paper), and 1.08×10^7 kg/m^{4}s for our model.

The magnitude plot, on the left, shows good agreement between our model and the measurements from Hudde (1983), Farmer-Fedor and Rabbitt (2002), and Voss and Allen (1994). The two models from OP08 show serious discrepancies with normal data: they lack normal stiffness at low frequencies and show unusual ripples at and above 1 kHz.

The phase plots show this discrepancy in an even more obvious manner. Our model, as well as the measurements from Hudde (1983), Farmer-Fedor and Rabbitt (2002), and Voss and Allen (1994), have linear phase, with a slope which characterizes the round-trip delay. However, the phases from OP08 are non monotonic, which demands several reflection sites along the propagation path: namely, the sound wave is trapped between those reflection sites, causing an increase in the overall system delay. This last observation is consistent with our previous analysis of the transfer function delay.

4. Discussion

4.1. Velocimetry and reflectance

On the one hand, we have observed that our model reasonably matches reflectance data, even when it is compared to data not used for the model parameters estimation; however, the agree-

ment is less clear regarding middle ear transfer functions. On the other hand, a model which has been designed to fit middle ear transfer functions seems to fail to match the reflectance data.

This observation raises the following important question: are ossicle temporal bone velocity measurements compatible with normal (living ears) impedance measurements? Temporal bone velocimetry is an invasive measurement and its properties seem to differ from living ears, especially when they have been frozen. The OP08 study also reports velocimetry in living ears (Huber et al., 2001) but those measurements are performed during clinical surgery, hence with altered ears. The key difference seems to reside in the middle ear delay; in fact, velocimetry measurements provided here, and referenced by O'Connor and Puria (2008) show much larger delays than typical live human impedance measurements.

We have run our simulation using middle ear parameters values from OP08 (see Section 2.3) and we did not get a normal middle ear impedance; in fact, using OP08 parameters added delay and compliance, and brought the first impedance minimum to much lower frequencies. We have tried to fit our model to the ME transfer function data shown in Section 3.6.1, but could not mimic the roll-off above 1 kHz, except by using a very large mass, which also resulted in a narrower bandwidth. We believe that it is not possible to obtain the behavior presented by OP08 with our model and physical values for its parameters. At this point, we cannot justify these differences, except that our model has been fitted to impedance data in living ears, while the OP08 model has been fitted to velocity measurements in temporal bones.

This discussion is limited to the OP08 model which has been fitted to a given measurement, and then used to simulate another. It would be better if we could rely on measurements performed in the same ear, showing both velocimetry and impedance or reflectance. Our guess is that such impedances would show a similar behavior.

4.2. Middle-ear delays

Delays in the middle ear have usually been computed from pressure or velocity measurements. With our model, it is possible to compute delays for only one component of the wave, and hence circumventing the complex interactions between the forward and backward waves (Neely and Allen, 2009). Indeed, the differences between our delays estimated on the forward wave (Section 3.1.1) and on the transfer functions (or "composite" delays) reveal that the two measures are not equivalent, due to standing wave interactions (pressure or impedance poles).

Unfortunately, forward and backward delays cannot be easily separated in experimental measures, and consequently composite delays are measured, not forward delays (though this separation is possible given the measured reflectance (Withnell et al., 2009)). Several publications (Scheperle et al., 2008; Withnell et al., 2009) have suggested that the cochlea pressure is best estimated from the input forward pressure, not the composite pressure, which includes the reflected wave. Thus, estimating the middle ear forward wave propagation time from the reflectance group delay seems like the better approach. As noted, this delay is the reflectance group delay, which is the time needed for the forward wave to reach the cochlea, and then return to the microphone (twice the forward delay).

4.3. Summary

The wave model presented here has originally been designed to match input impedance data from cat ears. Its parameters have been adjusted to take into account the anatomical differences between cats and humans, and to fit typical measurements from Voss

and Allen (1994), along with pathological middle ear data. The resulting simulations are presented in this study. Note that the model design has not been changed between the two studies. Overall, the model is in good agreement with experimental data from different sources and is able to capture the basic behavior of various common pathologies by merely adjusting its parameters, in a physical and meaningful way. The model is not ad-hoc: its design relies on well-established physics principles and its parameters values are consistent with previously-published similar models (Lynch et al., 1982; Puria and Allen, 1998; O'Connor and Puria, 2008). However, it is clear that it is still limited and cannot account for subtle natural variations observed in human data (i.e., above 5 kHz).

The goal of this study is not to compete with the accuracy of some recent models, especially those using finite-elements decomposition (Funnel and Decraemer, 1996; Fay, 2001). It is clear that those works are much more sophisticated and consequently are able to match experimental data to a greater extent. This work demonstrates that the time-domain wave-variable approach is valid to model the middle ear. It could eventually lead to significant improvements in the understanding of complex ear phenomena, cochlear non-linearities being one typical example (Sen and Allen, 2006).

A key feature of our modeling approach is the ability to discriminate between the forward and backward wave components. This opens the way to more detailed calculations on each of the components, and especially the forward wave. This study has underlined the possibility to estimate the propagation delay in the canal to the eardrum, but also on the TM and in the ossicles. Appreciating the propagation properties of the forward wave appears to be a promising idea to understand the canal response, and in particular its standing wave (Scheperle et al., 2008; Withnell et al., 2009), and a time-domain approach seems very relevant in this regard.

On a related note, it is our conviction that the issue of delays in the middle ear should be addressed more thoroughly. Our comparisons with data from temporal bones measurements reveal that usual impedance data may not be compatible with those, hence suggesting that the middle ear structure and behavior could be altered in subtle ways when performing velocimetry measurements on temporal bone preparations. A closely related question is the forward wave delay, compared to the composite (forward and reflected) wave delay, when standing waves are present.

One of the advantages of this approach is its simplicity: because it directly deals with wave components in the time domain, it is highly physical and intuitive. The implementation is simple enough so that the gist of it can easily be reproduced. This simplicity has a direct pay-off in terms of computation time and as a pedagogical tool. More specifically, we have built our approach on trying to simplify the TM to the greatest extent, though still taking into account its impedance-matching feature. The fact that, despite this extreme simplification, our model is able to reasonably match experimental data under many conditions, suggests that complex modes frequently observed on the TM are not critical to the behavior of the system.

References

Aibara, R., Welsh, J.T., Puria, S., Goode, R.L., 2001. Human middle-ear sound transfer function and cochlear input impedance. Hear. Res. 152, 100–109.
Allen, J.B., 1986. Measurement of eardrum acoustic impedance. In: Allen, J.B., Hall, J.L., Hubbard, A., Neely, S.T., Tubis, A. (Eds.), Peripheral Auditory Mechanisms. Springer-Verlag, New York, pp. 44–51.
Allen, J.B., Jeng, P.S., Levitt, H., 2005. Evaluating human middle ear function via an acoustic power assessment. J. Rehabil. Res. Dev. 42 (4), 63–78.
Bekesy, G.v., Rosenblith, W.A., 1951. The mechanical properties of the ear. In: Stevens, S.S. (Ed.), Handbook of Experimental Psychology. John Wiley and Sons Inc., New York.

Cheng, J.T., Aarnisalo, A.A., Harrington, E., del Socorro Hernandez-Montes, M., Furlong, C., Merchant, S.N., Rosowski, J.J., 2009. Stroboscopic holography measurement of motion of human tympanic membrane: a preliminary study. In: MEMRO Symposium, Stanford University, CA.

de La Rochefoucauld, O., Olson, E.S., 2009. A sum of simple and complex motions on the eardrum and manubrium in gerbil. In: MEMRO Symposium, Stanford University, CA.

Farmer-Fedor, B.L., Rabbitt, R.D., 2002. Acoustic intensity, impedance and reflection coefficient in the human ear canal. J. Acoust. Soc. Am. 112, 600–620.

Fay, J.P., 2001. Cat eardrum mechanics. PhD thesis, Stanford University.

Fay, J.P., Puria, S., Steele, C.R., 2002. Cat eardrum response mechanics. In: Pellegrino, S. (Ed.), Presented at the Calladine Festschrift. Kluwer Academic Publishers, The Netherlands.

Feeney, M.P., Grant, I.L., Marryott, L.P., 2003. Wideband energy reflectance measurements in adults with middle-ear disorders. J. Speech Lang. Hear. Res. 46 (4), 901–911.

Fletcher, H., Munson, W.A., 1933. Loudness, its definition, measurement and calculation. J. Acoust. Soc Am. 5, 82–108.

Funnel, W.R.J., Decraemer, W.F., 1996. On the incorporation of moire shape measurements in finite element models of the cat eardrum. J. Acoust. Soc. Am. 100 (2), 925–932. Part 1.

Funnel, W.R.J., Decraemer, W.F., Khanna, S.M., 1987. On the damped frequency response of a finite-element model of the cat eardrum. J. Acoust. Soc. Am. 81 (6), 1851–1859.

Funnel, W.R.J., Laszlo, C.A., 1978. Modeling of the cat eardrum as a thin shell using the finite-element method. J. Acoust. Soc. Am. 63, 1461–1466.

Giguere, C., Woodland, P.C., 1994. A computational model of the auditory periphery for speech and hearing research. i. ascending path. J. Acoust. Soc. Am. 95 (1), 331–342.

Gravel, J., 1999–2002. Acoustical power flow as an audiological tool. Otitis media with effusion data, collected in children at the Albert Einstein College of Medicine of Yeshiva University (New York, NY), by Dr. Judith Gravel and her team of audiologists. Study carried out under the subcontract of Mimosa Acoustics, Inc. (Champaign, IL), NIDCD SBIR Phase II Grant, No. R44 DC0313802. Unpublished data.

Guinan Jr., J.J., Peake, W.T., 1967. Middle-ear characteristics of anesthetized cats. J. Acoust. Soc. Am. 41 (5), 1237–1261.

Huber, A., Linder, T., Ferrazzini, M., Scmid, S., Dillier, N., Stoeckli, S., Fisch, U., 2001. Intraoperative assessment of stapes movement. Ann. Otol. Rhinol. Laryngol. 110, 31–35.

Hudde, H., 1983. Measurement of the eardrum impedance of human ears. J. Acoust. Soc. Am. 73, 242–247.

Hunter, L.L., Tubaugh, L., Jackson, A.e.a., 2008. Wideband middle ear power measurement in infants and children. J. Am. Acad. Audiol. 19 (4), 309–324.

Keefe, D.H., 1984. Acoustical wave propagation in cylindrical ducts: transmission line parameter approximations for isothermal and nonisothermal boundary conditions. J. Acoust. Soc. Am. 75 (1), 58–62.

Kelly, J.L., Lochbaum, C., 1963. Speech synthesis. In: Proceedings of the Fourth International Congress on Acoustics, chapter Paper G42, ICA, Copenhagen, pp. 1–4

Lynch III, T.J., Nedzelnitsky, V., Peake, W.T., 1982. Input impedance of the cochlea in cat. J. Acoust. Soc. Am. 72 (1), 108–130.

Neely, S., Allen, J.B., 2009. Retrograde waves in the cochlea. In: Cooper, N.P., Kemp, D.T. (Eds.), Proceedings of the 10th Mechanics of Hearing Workshop. World Scientific Publishing Co., Singapore, pp. 62–67.

Neely, S.T., Gorga, M.P., 1998. Comparison between intensity and pressure as measures of sound level in the ear canal. J. Acoust. Soc. Am. 104 (5), 2925–2934.

O'Connor, K.N., Puria, S., 2006. Middle ear cavity and ear canal pressure-driven stapes velocity responses in human cadaveric temporal bones. J. Acoust. Soc. Am. 120, 1517–1528.

O'Connor, K.N., Puria, S., 2008. Middle-ear model parameters based on a population of human ears. J. Acoust. Soc. Am. 123 (1), 197–211.

O'Connor, K.N., Tam, M., Blevins, N.H., Puria, S., 2008. Tympanic membrane collagen fibers: a key to high frequency sound conduction. The Laryngoscope 118 (3), 483–490.

Olson, E.S., 1998. Observing middle ear and inner ear mechanics with novel intracochlear pressure sensors. J. Acoust. Soc. Am. 103, 3445–3463.

Parent, P., Allen, J.B., 2007. Wave model of the cat tympanic membrane. J. Acoust. Soc. Am. 122 (2), 918–931.

Puria, S., Allen, J.B., 1998. Measurements and model of the cat middle ear: evidence of tympanic membrane acoustic delay. J. Acoust. Soc. Am. 104 (6), 3463–3481.

Rabbitt, R.D., Holmes, M.H., 1986. A fibrous dynamic continuum model of the tympanic membrane. J. Acoust. Soc. Am. 80 (6), 1716–1728.

Scheperle, R.A., Neely, S.T., Kopun, J.G., Gorga, M.P., 2008. Influence of in situ, sound-level calibration on distortion-product otoacoustic emission variability. J. Acoust. Soc. Am. 124 (1), 288–300.

Sen, D., Allen, J.B., 2006. Functionality of cochlear micromechanics – as elucidated by the upward spread of masking and two tone suppression. Acoust. Aust. 34 (1), 43–51.

Shaw, E.A.G., 1977. Eardrum representation in middle-ear acoustical networks. J. Acoust. Soc. Am. 62 (Suppl. 1), S102.

Shaw, E.A.G., Stinson, M.R., 1981. Network concepts and energy flow in the human middle ear. J. Acoust. Soc. Am. 69 (S44), S43.

Stinson, M.R., 1985. The spatial distribution of sound pressure within scaled replicas of the human ear. J. Acoust. Soc. Am. 78 (5), 1596–1602.

Stinson, M.R., Shaw, E., Lawton, B., 1982. Estimation of acoustical energy reflectance at the eardrum from measurements of pressure distribution in the human ear canal. J. Acoust. Soc. Am. 72, 766–773.

Voss, S.E., Allen, J.B., 1994. Measurement of acoustic impedance and reflectance in the human ear canal. J. Acoust. Soc. Am. 95 (1), 372–384.

Voss, S.E., Rosowski, J.J., Merchant, S.N., Peake, W.T., 2000. Acoustic responses of the human middle ear. Hear. Res. 150, 43–69.

Wegel, R.L., Lane, C.E., 1924. The auditory masking of one pure tone by another and its probable relation to the dynamics of the inner ear. Phy. Rev. 23, 266–285.

Withnell, R.H., Jeng, P.S., Waldvogel, K., Morgenstein, K., Allen, J.B., 2009. An in situ calibration for hearing thresholds. J. Acoust. Soc. Am. 125 (3), 1605–1611.

Zwislocki, J., 1957. Some impedance measurements on normal and pathological ears. J. Acoust. Soc. Am. 29 (12), 1312–1317.

Zwislocki, J., 1962. Analysis of the middle-ear function. Part I: Input impedance. J. Acoust. Soc. Am. 34 (8, part 2), 1514–1523.